Journal of Neural Engineering

PURPOSE-LED PUBLISHING™

ACCEPTED MANUSCRIPT • OPEN ACCESS

Ultra high-density, 4096-channel intraoperative neurophysiological brain mapping for functional localization of the human central sulcus

To cite this article before publication: Alexandra Fink Skular *et al* 2026 *J. Neural Eng.* in press https://doi.org/10.1088/1741-2552/aea70f

Manuscript version: Accepted Manuscript

Accepted Manuscript is "the version of the article accepted for publication including all changes made as a result of the peer review process, and which may also include the addition to the article by IOP Publishing of a header, an article ID, a cover sheet and/or an 'Accepted Manuscript' watermark, but excluding any other editing, typesetting or other changes made by IOP Publishing and/or its licensors"

This Accepted Manuscript is **© 2026 The Author(s). Published by IOP Publishing Ltd**.

As the Version of Record of this article is going to be / has been published on a gold open access basis under a CC BY 4.0 licence, this Accepted Manuscript is available for reuse under a CC BY 4.0 licence immediately.

Everyone is permitted to use all or part of the original content in this article, provided that they adhere to all the terms of the licence https://creativecommons.org/licences/by/4.0

Although reasonable endeavours have been taken to obtain all necessary permissions from third parties to include their copyrighted content within this article, their full citation and copyright line may not be present in this Accepted Manuscript version. Before using any content from this article, please refer to the Version of Record on IOPscience once published for full citation and copyright details, as permissions may be required. All third party content is fully copyright protected and is not published on a gold open access basis under a CC BY licence, unless that is specifically stated in the figure caption in the Version of Record.

View the article online for updates and enhancements.

This content was downloaded from IP address 112.204.172.67 on 30/09/2026 at 13:33

Title: Ultra high-density, 4096-channel intraoperative neurophysiological brain mapping for functional localization of the human central sulcus

Authors: Alexandra Fink Skular, BS,[1,2*] Gelana Tostaeva, BS,[1,2*] Elton Ho, PhD,[3] Jacqueline Dister, BS,[3] Daniel D. Cummins, MD,[4] Katrina Barth, PhD,[3] Lizbeth Nunez, MS,[4,5] Adam Poole, BS,[3] Craig H. Mermel, MD, PhD,[3] Benjamin Rapoport, MD, PhD,[3] Joshua B. Bederson, MD,[4†] Ignacio Saez, PhD[1,2,4,5†]

* These authors contributed equally
† Co-senior authors

Affiliations:
[1]Nash Family Department of Neuroscience, Icahn School of Medicine at Mount Sinai, New York, NY, USA.
[2]The Friedman Brain Institute, Icahn School of Medicine at Mount Sinai, New York, NY, USA.
[3]Precision Neuroscience Corporation, New York, NY, USA.
[4]Department of Neurosurgery, Icahn School of Medicine at Mount Sinai, New York, NY, USA.
[5]Nash Family Center for Advanced Circuit Therapeutics, Icahn School of Medicine at Mount Sinai, New York, NY, USA.

Corresponding Author:
Name and institution: Ignacio Saez; PhD, Icahn School of Medicine at Mount Sinai, New York, NY, USA. *Email*: ignacio.saez@mssm.edu

Keywords:
High-resolution µECoG (4096-channel), Central sulcus mapping, SSEP detection, Phase reversal, Brain-computer interface (BCI)

Accepted Manuscript

Abstract

Objective. Intraoperative localization of the central sulcus (CS) using somatosensory evoked-potential (SSEP) phase reversal is routinely performed with sparse subdural strip electrodes. We evaluated whether a multi-array, 4096-channel surface micro-electrocorticography (μECoG) configuration could provide dense two-dimensional sampling of stimulus-dependent sensorimotor responses within a standard neurosurgical workflow.

Approach. Four Precision Neuroscience Layer 7 μECoG arrays (1024 platinum electrodes per array on a flexible polyimide substrate, 400 μm electrode pitch, ~1.5 cm^2 active area per array) were deployed during resection of a right parafalcine meningioma in a 56-year-old male. Two arrays were placed horizontally on the exposed precentral gyrus; two were inserted under the intact dura overlying the postcentral gyrus, using a custom flexible stylet. SSEPs were recorded across five contralateral stimulation conditions (median nerve, ulnar nerve, index finger, middle finger, ring finger). Per-electrode SSEP responses were classified without anatomical labels, and spatial organization was quantified across stimulation conditions. Stimulus-locked high-gamma activity, digit-response maps, and signal quality across micro- and macroelectrodes were also evaluated.

Main results. Aggregate channel yield was 91.3% (3739/4096) at a 2 MΩ impedance criterion (per-array range 86.7–97.0%). Per-electrode amplitude maps resolved continuous phase-reversal contours with stimulus-specific spatial structure; reversal latencies were 19, 21, 25, 26, and 25 ms for median, ulnar, index, middle, and ring stimulation respectively. Phase reversal occurred within a single array in eight of ten sensory-array recordings, with the phase-reversal pattern varying across stimulation conditions. Digit responses showed measurable spatial differentiation within substantially overlapping response fields. Automated classification of the phase-reversal responses recovered the expected motor and sensory organization, consistent with the standard-of-care intraoperative localization performed in the same case.

Significance. The deployment shows that a four-array Layer 7 μECoG configuration can be used within a standard neurosurgical exposure and provides dense two-dimensional sampling of stimulus-dependent phase-reversal patterns across the peri-Rolandic recording field. The measured responses were correlated across approximately 3–4 mm of cortex, an order of magnitude coarser than the 400 μm electrode pitch, so the contribution demonstrated here is dense spatial sampling rather than submillimeter physiological resolution. Dense sampling rendered the polarity transition as a continuous two-dimensional boundary across the recording field rather than as a reversal between two adjacent contacts. The platform supports future evaluation of high-density surface μECoG for intraoperative mapping and chronic brain–computer-interface applications.

Accepted Manuscript

Introduction

Maximizing tumor resection while preserving sensorimotor function remains a central objective in neurosurgical oncology. When lesions are near the precentral or postcentral gyri, intraoperative neurophysiological monitoring complements anatomical navigation and helps reduce the risk of postoperative motor or sensory deficits [1–4]. The standard intraoperative protocol for central sulcus (CS) localization uses somatosensory evoked potential (SSEP) phase reversal: peripheral nerve stimulation elicits a positive deflection over precentral motor cortex (P20) and a negative deflection over postcentral somatosensory cortex (N20) at approximately 20 ms, and the polarity transition is used to infer the functional central sulcus [1,2,5–15].

This approach is widely used in surgical practice but is limited by the spatial sampling of conventional subdural strip electrodes. An 8-contact strip placed perpendicular to the presumed central sulcus can identify a reversal between neighboring contacts, but its effective spatial resolution is constrained by millimeter-scale contact diameter and pitch. In cases where anatomy is distorted or cortical exposure is constrained, including lesions associated with mass effect, shifted sulcal anatomy, or limited craniotomy exposure, standard strip recordings provide only sparse samples of the P20/N20 polarity transition, which may limit the spatial detail available for interpreting the functional boundary [16,17].

High-density surface micro-electrocorticography (μECoG) provides a means to increase spatial sampling by reducing contact pitch to hundreds of micrometers while remaining nonpenetrating and removable [18,19]. The Precision Neuroscience Layer 7 Cortical Interface is a flexible μECoG platform for high-density cortical recording from the cortical surface [20]. Recent work provided in-human demonstration of this platform establishing its intraoperative feasibility and high-density mapping of sensorimotor and language areas [21]. Another report from our group describes two-array mapping across the central sulcus in a separate case [22]. A single array, however, covers only approximately 1.5 cm^2; in peri-Rolandic mapping, multi-array coverage is needed to sample longer sections of the central sulcus boundary.

Here we report the intraoperative deployment of four Layer 7 arrays in a single surgical procedure, yielding 4096 total channels across motor and somatosensory cortex during resection of a right parafalcine meningioma. Our case establishes a new record to date for the highest number of simultaneously recorded μECoG channels in the human brain to our knowledge. We further demonstrate the feasibility of multi-array surface μECoG integration within a standard neurosurgical workflow and characterize large-scale intraoperative recording performance through analyses of channel yield, impedance distributions, and SSEP signal quality. We show that an automated, anatomically agnostic SSEP classification pipeline can identify motor, sensory, and phase-reversal responses consistent with established physiology across five peripheral nerve and digit stimulation conditions. We further examine the spatial information provided by dense two-dimensional sampling by quantifying stimulus-dependent phase-reversal patterns, digit-response organization, and the spatial scale of SSEP and high-gamma responses. Together, these results support the feasibility of high-density surface μECoG for dense intraoperative SSEP mapping and characterize the spatial information captured by a multi-array configuration.

Methods

Patient and Surgical Overview

A 56-year-old male with no significant medical history presented with left-sided hearing loss. Brain magnetic resonance imaging (MRI) showed a 2-cm right frontal parafalcine contrast-enhancing mass with moderate vasogenic edema, consistent with meningioma (**Fig. 1A**, left). He was neurologically intact at presentation. The patient underwent surgical resection given the lesion size, mass effect, and edema. A right frontoparietal craniotomy was performed using a standard interhemispheric approach. The tumor originated from the falx and extended laterally into the right cerebral cortex. Resection was performed through a corridor anterior to the

Accepted Manuscript

motor pathways, and gross total resection was achieved (**Fig. 1A**, right). The patient experienced transient left distal lower extremity weakness, which resolved completely within two weeks.

The patient provided written informed consent for the intraoperative research deployment and use of de-identified neural recordings. The study was approved by the Mount Sinai Institutional Review Board (protocol 22-01745).

The Layer 7 Cortical Interface

The Layer 7 Cortical Interface is a high-resolution, thin-film micro-electrocorticography (μECoG) array engineered for high-density, surface-level neural recordings (**Fig. 1B**). Each array contains 1024 electrodes: a rectangular main grid of 1019 electrodes (977 at 50 μm and 42 at 380 μm in diameter) at a 400 μm pitch, spanning ~1.5 cm² of active area, plus 5 additional contacts (500 μm in diameter) placed further outside the main grid for optional use for offline re-referencing. The arrays are fabricated on a flexible polyimide substrate using semiconductor microfabrication techniques, enabling conformal placement over the cortical surface without mechanical compression.

In this case, four arrays (4096 total channels) were deployed intraoperatively and connected to custom amplifier headstages. Neural data were acquired in real time at 20 kHz using a proprietary INTAN-based recording system optimized for high-bandwidth, low-noise electrophysiology [20,21]. Each array is referred to throughout by anatomical position: medial motor (MM), lateral motor (LM), medial sensory (MS), and lateral sensory (LS).

Array Positions on a Standard Brain Model

The four arrays were registered onto the FreeSurfer average template brain [23] using the preoperative MRI reconstruction together with the intraoperative photographs, and are shown in the dorsal view corresponding to the craniotomy (**Supplementary Fig. S1)**. The rendering establishes the arrangement of the four arrays relative to the central sulcus and the pre- and postcentral gyri rather than the position of any individual electrode on this patient's cortex.

Intraoperative Central Sulcus Mapping via SSEP

Central sulcus localization was initiated using a standard 8-contact subdural strip electrode (Ad-Tech Medical) positioned perpendicular to the presumed central sulcus to identify phase reversals from median nerve SSEPs, following established intraoperative neurophysiological monitoring (IONM) protocols [24,25]. After standard localization, four 1024-channel μECoG arrays were positioned around the central sulcus (**Fig. 1C** for array comparison). Two arrays were placed horizontally over the exposed precentral gyrus (motor cortex); the remaining two were inserted vertically beneath the skull and under the unexposed dura overlying the postcentral gyrus using a custom-built flexible stylet (**Fig. 1D**), since the craniotomy did not expose postcentral cortex due to the tumor's anterior location.

SSEPs were evoked sequentially by electrical stimulation of the contralateral median nerve, index finger, middle finger, ulnar nerve, and ring finger. Median nerve and index finger stimulation were performed during tumor resection, while remaining sites were stimulated after gross total resection (**Fig. 1E**). Stimulation parameters were standardized: single pulses at 1.41 Hz (709 ms inter-stimulus interval), 200 μs pulse width, and 20–40 mA amplitude. For each pulse, a TTL trigger was co-recorded with neural signals to enable averaging of stimulus-locked activity. SSEP responses were computed as trial-averaged neural signals. The total study duration did not exceed 15 minutes and did not interfere with the clinical procedure or surgical workflow. SSEP responses from the μECoG array were collected for research purposes only and not used for any clinical decision making intraoperatively.

SSEP Data Preprocessing

Accepted Manuscript

Neural data were preprocessed using a standardized pipeline. Raw signals were downsampled from 20 kHz to 2 kHz via polyphase resampling (SciPy) to reduce computational load while preserving signal fidelity. Channels with impedances >2 MΩ were excluded. Signals were bandpass filtered from 30–250 Hz using a second-order Butterworth filter to isolate cortical activity and suppress low-frequency drift [24–27].

SSEPs were computed by averaging across epochs for each of the 1024 channels. Epoch counts per condition were median nerve (n = 110), ulnar nerve (n = 160), index finger (n = 110), middle finger (n = 120), and ring finger (n = 150). To normalize responses, baseline correction was applied using the pre-stimulus window (−80 to −30 ms): the mean was subtracted and the result divided by the baseline standard deviation (SD), yielding z-scored SSEPs for each channel [27–32]. All amplitude values reported are unitless z-scores relative to the local pre-stimulus noise floor, not raw microvolt amplitudes.

Automated Detection and Classification of High-Resolution SSEPs

To assess automated classification of short-latency somatosensory evoked potentials (SSEPs), we developed an offline detection algorithm that operated independently of anatomical ground truth. For each electrode, peak detection was performed on the z-scored, trial-averaged SSEP waveform within a 5–32.5 ms post-stimulus window. Positive and negative peaks were detected using a z-score height threshold of 3. Channel polarity was assigned from the second-largest suprathreshold detected peak, rather than the largest peak, to reduce the influence of residual artifact at the masked window edge. Channels with fewer than two suprathreshold peaks were assigned no polarity and excluded from subsequent classification.

After per-channel classification, outlier rejection retained only channels whose waveform shape correlated with the mean waveform of the corresponding polarity class (Spearman r >= 0.5). For each retained channel, the pipeline extracted peak amplitude, peak latency, and peak-to-peak measures. The automated workflow is summarized in **Fig. 2.**

Array-Level Classification and Phase Reversal Detection

Each array-stimulation recording was classified as P20-dominant, N20-dominant, phase reversal (PR), or no SSEP detected. Classification was performed independently for each array and stimulation condition, without using anatomical labels. To reduce classifications driven by sparse detections, P20- or N20-dominant assignment required at least 20 suprathreshold classified channels and at least 7.5% of all recording channels to meet the corresponding polarity criterion (for a 1024-channel array, at least 77 channels). For an array to be classified as exhibiting a phase reversal, both P20 and N20 classes had to be present with at least 20 channels each, and the phase-reversal ratio (PRR) had to exceed 0.10:

$$PRR = \frac{P_{20}}{P_{20} + N_{20}} \times \frac{N_{20}}{P_{20} + N_{20}}$$

PRR quantifies the product of the P20 and N20 response proportions among responsive channels. Values approach 0 when one polarity predominates and reach a maximum of 0.25 when P20 and N20 responses are equally represented. Thus, PRR provides an operational measure of mixed-polarity response structure, as expected when an array samples the electrophysiological phase reversal across the central sulcus. Arrays that did not meet criteria for P20 dominance, N20 dominance, or phase reversal were labeled as no SSEP detected. This framework enabled standardized classification across arrays and peripheral nerve stimulation conditions and provided the basis for subsequent analysis of spatial SSEP topography.

Single-Trial Classification of Stimulus Conditions

Accepted Manuscript

Single-trial classification was used to identify the peripheral stimulation condition from the recorded response. Separate classifiers distinguished median from ulnar nerve stimulation, the three digit conditions (index, middle, ring), and all five stimulation conditions. Recordings were epoched from −120 to +120 ms relative to stimulus onset. For each channel and trial, high-gamma activity was computed as the Hilbert envelope of the 70–200 Hz signal after fourth-order Butterworth bandpass filtering, implemented in second-order sections and applied forward and backward. The envelope was averaged over 15–32 ms post-stimulus, and the mean from the same trial's −52 to −30 ms pre-stimulus baseline was subtracted. A spatial-pattern feature was generated by subtracting the across-channel mean and dividing by the across-channel standard deviation for each trial. A separate classifier was trained on global response magnitude, specifically the high-gamma response averaged across all channels. Spatial-pattern classification was compared with global-magnitude classification to assess the contribution of the spatial distribution of the response. The same feature extraction was applied to a −24 to −4 ms pre-stimulus window as a within-recording null control. Throughout, baseline refers to the −52 to −30 ms interval used for trial-wise subtraction, whereas pre-stimulus null refers to the −24 to −4 ms control window used for classification.

Classification was performed using shrinkage linear discriminant analysis (LDA), with covariance shrinkage of 0.5 toward a scaled identity matrix. Feature standardization was estimated from the training data within each fold. Performance was evaluated using stratified five-fold cross-validation repeated three times. Channels that failed the impedance criterion or contained non-finite values in any trial were excluded. All delivered stimuli were retained, with no trial rejection based on signal amplitude or quality. Trial counts varied across conditions (median nerve, 106–112; ulnar nerve, 160–165; digits, 106–154). Performance was therefore reported as balanced accuracy, calculated as the mean per-class recall, with chance level equal to 1/K for K classes. Nerve- and digit-classification analyses used common-average referencing across the array.

For time-resolved classification, LFP (5–250 Hz) and high-gamma features were concatenated within a 12 ms window advanced in 4 ms steps. Both signals were filtered using the fourth-order, forward-and-backward Butterworth implementation described above.

High-Gamma Response and Spatial Scale

High-gamma activity was quantified as described above. Inter-trial phase coherence was computed as the magnitude of the trial-mean unit-magnitude analytic phasors. Here we report high-gamma activity as stimulus-locked. Spatial coherence length was defined as the inter-electrode distance at which the spatial autocorrelation of the response map fell to half its zero-distance value and is reported for the response sampled within the 1.5 cm^2 array area.

Spatial Organization of Digit Responses

Spatial maps were generated from the class mean of the per-trial baseline-corrected high-gamma feature used for classification. For each digit, the peak region was defined as the top 20% of response values. Location was quantified as the centroid of this region weighted by the response amplitude at each channel, spatial extent as the 1σ covariance ellipse computed with the same weights, and pairwise overlap using the Dice coefficient [33]. Spatial separation was quantified as the mean pairwise distance between digit centroids and compared with a null distribution generated by permuting digit labels across pooled single trials and recomputing the class means and centroid distances (2,000 permutations). The analysis was performed separately for high-gamma activity, mapped as the class-mean baseline-corrected envelope, and for the SSEP, mapped as the maximum absolute deflection within the response window relative to the pre-stimulus baseline.

Macroelectrode and Microelectrode Comparison

Each array contains 42 macroelectrodes (380 μm diameter) distributed among the 50 μm microelectrodes. Because the two contact types are not uniformly interleaved, each macroelectrode was compared with the mean

Accepted Manuscript

of the microelectrodes within 1 mm, yielding 162 co-located pairs. The comparison used the median-nerve condition and included channels passing the pre-recording impedance criterion; impedance was obtained from the same check. SSEP amplitude was quantified as the peak-to-peak amplitude of the trial-averaged response. Baseline noise was quantified as the standard deviation of the pre-stimulus signal (−80 to −10 ms) in the 30–250 Hz and 300–500 Hz bands. The 30–250 Hz measure was used as the denominator for SSEP signal-to-noise ratio (SNR), while the 300–500 Hz measure was used for the high-frequency noise comparison.

Equivalence was assessed using two one-sided tests. Equivalence margins were ±15% of the microelectrode median for SSEP amplitude and 300–500 Hz noise and ±0.10 for signal-to-noise ratio, which had a microelectrode median of 0.90. The margins were selected after inspection of the descriptive distributions and were not pre-specified.

Control Analyses for Single-Trial Classification

Because each stimulation condition was acquired in a separate recording, additional analyses assessed whether classification could be explained by between-recording differences rather than stimulus-locked responses. Randomly timed pseudo-trials were sampled within each recording, at least 400 ms from any stimulus and matched in number to the stimulus-locked trials, and passed through the same classification pipeline. Classification was also repeated using an acquisition-order split rather than stratified cross-validation, with the first 75% of each recording used for training and the final 25% for testing, and over early post-stimulus windows (0–8, 4–12, and 8–16 ms) to assess classification before the expected cortical response. To assess slow temporal drift directly, the first and second halves of trials within each recording were treated as pseudo-conditions and classified using the same pipeline.

Acquisition timestamps confirmed that the two sensory arrays were recorded simultaneously for each stimulation condition, as were the two motor arrays. Finally, pairwise classifications were compared according to whether the two conditions were acquired within the same surgical period or across tumor resection. Median nerve and index finger stimulation were acquired during resection, whereas ulnar nerve, middle finger, and ring finger stimulation were acquired after gross total resection.

Results

Channel Yield and Impedance Supported Multi-Array Recording Quality

Aggregate channel yield was 91.3% (3739/4096 channels retained). Per-array yields were 88.2% for MM (903/1024 retained; 121 omitted), 86.7% for LM (888/1024; 136 omitted), 97.0% for MS (993/1024; 31 omitted), and 93.3% for LS (955/1024; 69 omitted) (**Supplementary Fig. S2**). Mean impedance among retained channels was 1251 kΩ for MM, 1543 kΩ for LM, 1062 kΩ for MS, and 1140 kΩ for LS (**Supplementary Fig. S2**). Because impedance is an electrode-level property, these denominators refer to the four 1024-channel arrays rather than channels multiplied by the number of stimulation recordings.

High-Resolution Cortical Mapping of SSEP Waveforms

The automated detection pipeline identified short-latency SSEP components across the high-density recordings (**Fig. 2A).** Representative median nerve SSEP waveforms from each array revealed consistent temporal features, including a distinct early deflection at ~20 ms post-stimulus (**Fig. 2B**). LM and LS arrays showed the largest signal amplitudes, with prominent N20 or P20 components depending on cortical location. A clear polarity reversal between motor (anterior) and sensory (posterior) arrays was consistent with the known cytoarchitecture across the central sulcus. The largest responses were observed near the LM–LS boundary, consistent with the array placement across peri-Rolandic cortex.

Accepted Manuscript

A subset of spatially ordered traces (**Fig. 2C**) revealed a smooth transition in waveform morphology across the medial-to-lateral and motor-to-sensory axes. Quantitatively, the early SSEP peaked at ~20 ms post-stimulus, with N20 components localized to the sensory (LS, MS) arrays and P20 components to the motor (LM, MM) arrays. Per-stimulation peak amplitudes and latencies for all classified channels are reported in Table 1 and Fig. 3B,C,E,F; consistent with the z-scoring described in Methods, amplitudes are unitless z-scores relative to each channel's pre-stimulus baseline rather than microvolt values.

Classification of individual waveforms into N20- or P20-dominant responses revealed 81.7% of waveforms in LS and MS arrays were classified as N20-dominant, while 77.3% of LM and MM waveforms were classified as P20-dominant **(Fig. 2D**). The sharp transition in polarity occurred along the LM–LS array boundary, corresponding to the presumed location of the central sulcus and consistent with the expected motor-sensory organization.

P20 and N20 Morphology Varied Across Stimulation Conditions

Next, we examined the evoked waveforms across stimulation conditions: median nerve, ulnar nerve, and individual digits (index, middle, ring). Morphological analysis of P20 and N20 waveforms revealed distinct neurophysiological signatures (**Fig. 3; Table 1**). Proximal nerve stimulation produced earlier and larger z-scored responses than digit stimulation, whereas digit stimulation produced later responses with different spatial response patterns in the spatial maps (**Fig. 5A**). Because all plotted amplitudes were computed from pre-stimulus z-scored data, amplitude comparisons reflect evoked-response signal-to-noise relative to each channel's baseline, not absolute microvolt voltage.

Waveform morphology, peak amplitude, and peak latency for each stimulation condition are shown in **Fig. 3A-F**, consistent with the differential N20/P20 dominance observed across sensory and motor arrays (**Fig. 2D**). Pooled across arrays, peak amplitudes exceeded the $z = 3$ detection threshold across all classified channel-stimulation observations. The strongest proximal-nerve contrast was observed for ulnar stimulation, where P20 channels reached a median absolute peak amplitude of approximately $|z| = 55$. Because z-scored amplitude is referenced to each channel's pre-stimulus noise floor, which narrows as more trials are averaged, cross-stimulation amplitude differences are shaped by epoch count as well as physiology: ulnar nerve and ring finger stimulation contributed the most epochs ($n = 160$ and $n = 150$) versus median nerve and index finger ($n = 110$ each) and middle finger ($n = 120$). The larger z-scored responses for ulnar and ring stimulation therefore reflect a combination of evoked-response strength and the higher signal-to-noise afforded by their greater trial counts, and cross-condition amplitudes should not be read as a purely physiological ranking. The per-array summary figure further stratified SSEP morphology by array and stimulation condition (**Fig. 4).** Per-array grand-mean morphology across all stimulation conditions is shown in Supplementary Fig. S3.

High-Density Spatial Maps Showed Stimulus-Specific Phase-Reversal Structure

Per-electrode spatial maps at phase-reversal latencies showed stimulus-specific polarity structure across the four arrays (**Fig. 5**). Each stimulation condition evoked a distinct and spatially localized phase-reversal boundary (**Fig. 5A**). Median nerve stimulation produced the earliest and most extensive response, with a robust and continuous phase reversal observed at ~19 ms post-stimulus, and ulnar stimulation elicited a similar pattern at ~21 ms. Stimulation of individual digits produced reversals at longer latencies, with peak responses at 25 ms for the index finger, 26 ms for the middle finger, and 25 ms for the ring finger, together with the differences in the location of the phase-reversal boundary (**Supplementary Fig. S5A**). The direction of those differences is not quantified from these maps; the quantitative comparison of digit response location is reported below. These differences highlight that the phase-reversal pattern varied across stimulation conditions in both space and time. These maps support dense visualization of the phase-reversal field.

The polarity maps were consistent with array placement and expected physiology. Overlaying phase-reversal contours on the surgical field (**Fig. 5B**) revealed differences in contour locations and geometry across stimulation

Accepted Manuscript

conditions. Median and ulnar nerve responses projected to overlapping but distinct regions along the postcentral gyrus. Digit-specific phase-reversal boundaries differed from one another in location and geometry, and the boundaries traced by finger stimulation ran orthogonal to the central sulcus. Phase-reversal contours frequently crossed individual arrays, allowing the polarity transition to be sampled as a two-dimensional spatial pattern. These data indicate that phase reversal mapping using high-density surface arrays captures the stimulus-dependent spatial structure across the sensorimotor recording field.

Full per-electrode waveform grids are shown in **Supplementary Fig. S4**. Supplementary Video 1 shows the time-resolved phase-reversal maps.

Array-Level Classification Was Largely Stable Across Downstream Threshold Perturbations

Array-level classification across the 4 × 5 array–stimulation grid was concordant with the expected sensorimotor organization. Both motor arrays (MM and LM) were classified as P20-dominant for all five stimulation conditions, while the sensory arrays (MS and LS) were classified as N20-dominant or phase reversal in all ten of their array–stimulation recordings — recovering the same motor–sensory boundary resolved by the per-electrode spatial maps and consistent with the standard-of-care strip localization performed in the same case. Eight of the ten sensory-array recordings were classified as phase reversal, placing the polarity transition within a single array. The two sensory arrays differed in which stimulation conditions produced phase reversal: LS was N20-dominant for median-nerve stimulation but showed phase reversal for the other four conditions, whereas MS showed phase reversal for median-nerve stimulation and was N20-dominant for index-finger stimulation (**Supplementary Fig. S5B).** Together, the two arrays sampled stimulus-dependent variation in the phase-reversal pattern across a broader cortical extent than either array alone. The phase-reversal ratio (PRR) supported these assignments: every sensory-array recording classified as phase reversal had a higher PRR than any motor-array recording in this case, and the classification grid was stable under downstream threshold perturbation apart from two borderline cells. The full classification grid, per-recording PRR values, and the threshold-sensitivity analysis are provided in **Supplementary Fig. S5.**

Digit Responses Showed Spatially Structured, Overlapping Patterns

Digit-response maps showed differences in spatial organization across stimulation conditions (**Supplementary Fig. S6).** Peak-response regions overlapped substantially, with pairwise Dice coefficients of 0.21–0.74 for SSEP maps and 0.22–0.87 for high-gamma maps. SSEP centroids were more separated than expected under label permutation on all four arrays ($p \leq 0.03$). High-gamma centroids were significantly separated on the two lateral arrays (both $p < 0.001$), but not on the medial arrays ($p = 0.13$ and 0.34). Centroid locations did not show a consistent index-to-ring ordering across arrays.

These results show measurable spatial differentiation among digit responses within substantially overlapping response fields.

Stimulus-Locked High-Gamma Co-Localized with the SSEP

Stimulus-locked high-gamma activity (70–200 Hz) increased following stimulation, reaching 3.7-fold above the pre-stimulus level on the highest-SNR array. The response was also phase-locked across trials: median inter-trial phase coherence was 0.885 (IQR, 0.850–0.901) on the lateral sensory array and 0.765 on the medial motor array. Spatially, high-gamma activity co-localized with the low-frequency SSEP, with similar coherence lengths (3.4–3.8 mm for high-gamma and 3.4–4.2 mm for the SSEP). No finer spatial structure was evident in the high-gamma response at the scale sampled here.

Single-Trial Spatial Patterns Distinguished Stimulation Conditions

Accepted Manuscript

Single-trial high-gamma spatial patterns discriminated stimulation conditions (**Fig. 6B,C**). Median versus ulnar nerve stimulation was classified with balanced accuracies of 0.95–0.99 on three of four arrays (chance, 0.50), while three-way digit classification (index, middle, ring) reached 0.77–0.94 (chance, 0.33).

Classification was at chance before stimulation and increased within the 15–32 ms post-stimulus response window (**Fig. 6A**). The control analyses for between-recording differences were also at chance: classification from a matched pre-stimulus window reached 0.47–0.50 for nerve and 0.30–0.34 for digits against chance levels of 0.50 and 0.33 (Fig. 6C, hatched bars), randomly timed pseudo-trials drawn from the same recordings reached 0.42–0.51, and pseudo-conditions formed by splitting each recording into its first and second halves, thus differing only in acquisition time, averaged 0.55 (range 0.38–0.65) across the 20 array × condition recordings. After removing each trial's spatial mean and scale, nerve classification remained at 0.94–0.99 on the three responsive arrays. Classification using only the whole-array mean amplitude was 0.45–0.54 on three arrays and 0.70 on the medial motor array. For digit stimulation, mean-amplitude classification reached 0.55–0.64, compared with 0.77–0.94 using the spatial pattern (**Fig. 6D**). Because each stimulation condition was acquired in a separate recording, these results quantify between-condition discriminability rather than stimulus identification within a common recording.

Macroelectrode and Microelectrode Signal Quality

For the median-nerve condition, 380 μm macroelectrodes were compared with the mean of neighboring 50 μm microelectrodes across 162 co-located pairs (**Supplementary Fig. S7).** Despite the substantially higher impedance of the microelectrodes, SSEP signal-to-noise ratio and 300–500 Hz pre-stimulus noise fell within the tested equivalence margins. SSEP amplitude was 1.25 μV higher on average for the macroelectrodes (8.4% of the microelectrode median) and remained within the ±15% equivalence margin.

Discussion

This single-case evaluation shows that four high-density Layer 7 surface μECoG arrays can be deployed during a standard neurosurgical procedure and can provide high-channel-count SSEP recordings suitable for dense mapping of the central sulcus phase reversal. The device achieved 91.3% aggregate channel yield (<2 MΩ impedance), recorded short-latency evoked responses across nerve and finger stimulation, and supported an anatomically agnostic descriptive classification pipeline whose labels were concordant with expected motor, sensory, and phase-reversal organization.

The multi-array deployment of flexible Layer 7 arrays demonstrates a technical strategy for increasing high-density cortical coverage within the constraints of a standard neurosurgical exposure. Two arrays were placed on exposed precentral cortex, while two were advanced subdurally toward postcentral cortex using a custom flexible stylet. This addresses a practical problem in surgical neurotechnology: craniotomies are planned for lesion access and patient safety rather than ideal device coverage. In this case, stylet-assisted placement allowed the recording field to sample cortex beyond the directly exposed cortical window.

The present study extends conventional SSEP phase-reversal mapping from millimeter-scale strip contacts to dense two-dimensional sampling on a 400 μm grid, changing the central sulcus readout from a pairwise polarity reversal to a dense spatial polarity map. These contributions align with prior work on automated central sulcus localization and high-resolution cortical mapping [6,13,21], while the four-array configuration expands simultaneous coverage compared with single-array deployments [21]. Phase-reversal patterns varied in both spatial location and temporal latency depending on the stimulation condition. Phase reversal occurred within a single array in eight of ten sensory-array recordings, with different stimulation conditions producing phase reversal on the two sensory arrays. Thus, the phase-reversal pattern sampled by the arrays was not identical across stimulation conditions. Together, these findings show that dense two-dimensional sampling provides information about the location and contour of the polarity transition beyond identifying a single reversal between neighboring contacts.

Accepted Manuscript

The additional analyses characterize the spatial structure of the recorded responses. Digit response regions overlapped substantially, while their centroids were separated beyond the label-shuffled null for SSEP responses on all four arrays and for high-gamma responses on the two lateral arrays. Centroid ordering was not consistent across arrays. Digit-related responses were therefore spatially structured but distributed across overlapping cortical regions rather than confined to isolated response sites. Stimulus-locked high-gamma activity showed a spatial scale similar to the low-frequency SSEP rather than finer spatial structure.

Single-trial high-gamma patterns also distinguished stimulation conditions. Classification remained high after removing each trial's spatial mean and scale and generally exceeded classification based on whole-array response magnitude alone, indicating that the spatial distribution of the response contributed to classification. However, because each stimulation condition was acquired in a separate recording, stimulus identity was confounded with recording identity. This analysis therefore demonstrates between-condition discriminability of the recorded spatial patterns, not real-time identification of stimuli within a common recording.

The evoked fields had spatial coherence lengths of approximately 3.4–4.2 mm, considerably larger than the 400 μm electrode pitch. Despite their substantially higher impedance, co-located 50 μm microelectrodes and 380 μm macroelectrodes showed comparable SSEP signal-to-noise and high-frequency baseline noise within the tested equivalence margins. For the SSEP responses examined here, the contribution of the dense microelectrode grid therefore lies primarily in spatial sampling rather than improved per-contact signal quality, and electrode pitch should not be equated with physiological spatial resolution. For routine central sulcus localization, these data do not yet establish an advantage over a conventional strip, and we do not propose the configuration used here as a better method for that task.

Dense two-dimensional sampling also differs from conventional strip recording in its sampling geometry. A strip resolves the reversal between adjacent contacts at one position; sampling how the response varies along the precentral gyrus would require repeated repositioning along the central sulcus. A high-contact flexible two-dimensional array samples this variation in a single placement. The complexity of the present deployment partly reflects the configuration used in this proof-of-concept study, including the use of four arrays, stylet-assisted placement, and high-channel-count acquisition hardware. Future implementations could use a single large-coverage conformable array, reduce cabling through on-device signal processing, and display a two-dimensional response map directly to the surgeon. Whether this additional spatial information improves intraoperative mapping or clinical outcomes will require direct comparative evaluation.

Several limitations should be acknowledged. This is a single-subject study, and while reproducibility was observed across multiple nerve conditions and arrays, broader generalization will require multi-subject validation. The present analysis was conducted offline after the surgical procedure; real-time intraoperative translation remains to be demonstrated. Stimulation order also followed surgical timing rather than randomization: median nerve and index finger were delivered during tumor resection, whereas ulnar nerve, middle finger, and ring finger were delivered after gross total resection. The control analyses address several potential sources of between-recording structure but cannot eliminate this design limitation.

Future studies should include multi-subject validation, direct comparison with conventional intraoperative mapping, and real-time implementation to determine whether the additional spatial information provided by dense two-dimensional sampling improves intraoperative mapping. Beyond intraoperative mapping, the stimulus-specific spatial structure observed here may also be relevant to surface sensorimotor BCI applications. The present study evaluated intraoperative evoked responses rather than voluntary-task classification, chronic recording stability, or somatosensory feedback, and these applications will require separate evaluation.

Conclusions

In this study, high-density, flexible μECoG arrays deployed intraoperatively supported anatomically agnostic, automated classification of short-latency somatosensory evoked potentials across the human sensorimotor

Accepted Manuscript

cortex. Dense two-dimensional sampling revealed stimulus-dependent spatial structure in the SSEP phase reversal and spatially structured, overlapping digit responses. Phase-reversal contours varied across stimulation conditions and frequently traversed the cortical area sampled by a single array, allowing the polarity transition to be characterized as a two-dimensional spatial pattern rather than only a reversal between neighboring contacts. These findings demonstrate that multi-array μECoG can densely characterize stimulus-dependent peri-Rolandic response fields across a broader cortical area than a single array, while the clinical value of this additional spatial information remains to be established through direct comparative study.

Accepted Manuscript

Conflict of Interest. Co-authors E. Ho, J. Dister, K. Barth, A. Poole, C. Mermel, and B. Rapoport are employees of Precision Neuroscience Corporation, the manufacturer of the Layer 7 Cortical Interface used in this study. B. Rapoport is a co-founder of Precision Neuroscience Corporation. A. Fink Skular, G. Tostaeva, D. Cummins, L. Nunez, J. B. Bederson, and I. Saez declare no competing interests.

Ethics. This study was approved by the Mount Sinai Institutional Review Board (protocol 22-01745) and was conducted in accordance with the principles of the Declaration of Helsinki and applicable local regulations. The patient provided written informed consent for intraoperative use of the research device, for use of de-identified neural recordings, and for publication of the de-identified intraoperative images.

Funding. The Layer 7 devices and on-site technical support were provided by Precision Neuroscience Corporation.

Data Availability. Reasonable requests for noncommercial research use of human electrophysiologic and other deidentified human clinical data will be considered and should be made to the corresponding author. Some restrictions apply to the availability of the data, due in part to patient confidentiality, and additional ethics review may be required.

Acknowledgments. We thank the operating-room and intraoperative-neurophysiological-monitoring staff at Mount Sinai for support during the surgical procedure and the patient and family for consenting to participate in this research deployment. A portion of this work was presented as a poster by Alexandra Fink Skular at the North American Neuromodulation Society Conference in Orlando, Florida, in 2025.

Author Contributions. A. Fink Skular: Methodology, Software, Formal analysis, Investigation, Writing – original draft. G. Tostaeva: Software, Formal analysis, Validation, Visualization, Writing – review & editing. E. Ho, J. Dister, K. Barth, A. Poole, C. H. Mermel, and B. Rapoport: Resources related to the device, on-site investigation support, Writing – review & editing. D. D. Cummins and L. Nunez: Investigation, Writing – review & editing. J. B. Bederson: Conceptualization, Resources, Investigation, Project administration, Writing – review & editing. I. Saez: Conceptualization, Supervision, Project administration, Funding acquisition, Writing – review & editing.

Accepted Manuscript

References

[1] Sloan T B 1997 Evoked potential monitoring of the central nervous system intraoperatively *Anesthesiology Clinics of North America* **15** 593–611

[2] López J R 2004 The use of evoked potentials in intraoperative neurophysiologic monitoring *Physical Medicine and Rehabilitation Clinics of North America* **15** 63–84

[3] Jameson L C and Sloan T B 2012 Neurophysiologic monitoring in neurosurgery *Anesthesiology Clinics* **30** 311–31

[4] You H and Qiao H 2021 Intraoperative neuromonitoring during resection of gliomas involving eloquent areas *Frontiers in Neurology* **12** 658680

[5] Grant G A, Farrell D and Silbergeld D L 2002 Continuous somatosensory evoked potential monitoring during brain tumor resection: Report of four cases and review of the literature *Journal of Neurosurgery* **97** 709–13

[6] Asman P, Prabhu S, Bastos D, Tummala S, Bhavsar S, McHugh T M and Ince N F 2021 Unsupervised machine learning can delineate central sulcus by using the spatiotemporal characteristic of somatosensory evoked potentials *Journal of Neural Engineering* **18** 046038

[7] Allison T, McCarthy G, Wood C C, Darcey T M, Spencer D D and Williamson P D 1989 Human cortical potentials evoked by stimulation of the median nerve. II. Cytoarchitectonic areas generating short-latency activity *Journal of Neurophysiology* **62** 694–710

[8] Wood C C, Spencer D D, Allison T, McCarthy G, Williamson P D and Goff W R 1988 Localization of human sensorimotor cortex during surgery by cortical surface recording of somatosensory evoked potentials *Journal of Neurosurgery* **68** 99–111

[9] Emerson R G and Pedley T A 1984 Generator sources of median somatosensory evoked potentials *Journal of Clinical Neurophysiology* **1** 203–18

[10] Yamada T, Yeh M and Kimura J 2004 Fundamental principles of somatosensory evoked potentials *Physical Medicine and Rehabilitation Clinics of North America* **15** 19–42

[11] Romstöck J, Fahlbusch R, Ganslandt O, Nimsky C and Strauss C 2002 Localisation of the sensorimotor cortex during surgery for brain tumours: Feasibility and waveform patterns of somatosensory evoked potentials *Journal of Neurology, Neurosurgery & Psychiatry* **72** 221–9

[12] Iwasaki M, Nair D and Lüders H O 2003 Cortical somatosensory evoked potential mapping *Presurgical assessment of the epilepsies with clinical neurophysiology and functional imaging* Handbook of clinical neurophysiology vol 3 (Elsevier) pp 287–95

[13] Xie T, Wu Z, Schalk G, Tong Y, Vato A, Raviv N, Guo Q, Ye H, Sheng X, Zhu X, Brunner P and Chen L 2022 Automated intraoperative central sulcus localization and somatotopic mapping using median nerve stimulation *Journal of Neural Engineering* **19** 046020

[14] Raffin E, Pellegrino G, Di Lazzaro V, Thielscher A and Siebner H R 2015 Bringing transcranial mapping into shape: Sulcus-aligned mapping captures motor somatotopy in human primary motor hand area *NeuroImage* **120** 164–75

[15] Simon M V 2013 Intraoperative neurophysiologic sensorimotor mapping-a review *Journal of Neurology & Neurophysiology* **4**

Accepted Manuscript

[16] Epstein N E, Danto J and Nardi D 1993 Evaluation of Intraoperative Somatosensory-Evoked Potential Monitoring During 100 Cervical Operations: *Spine* **18** 737–47

[17] Seyal M and Mull B 2002 Mechanisms of Signal Change During Intraoperative Somatosensory Evoked Potential Monitoring of the Spinal Cord: *Journal of Clinical Neurophysiology* **19** 409–15

[18] Geukes S H, Branco M P, Aarnoutse E J, Bekius A, Berezutskaya J and Ramsey N F 2024 Effect of Electrode Distance and Size on Electrocorticographic Recordings in Human Sensorimotor Cortex *Neuroinform* **22** 707–17

[19] Yuan Y, Zhang Y, Song X, Zhang X, Li C, Yuan T, Qi H and Yan L 2023 Value of multi-channel somatosensory evoked potentials recording in patients undergoing scoliosis correction surgery *Eur Spine J* **32** 4045–53

[20] Hettick M, Ho E, Poole A J, Monge M, Papageorgiou D, Takahashi K, LaMarca M, Trietsch D, Reed K, Murphy M, Rider S, Gelman K R, Byun Y W, Hanson T, Tolosa V, Lee S-H, Bhatia S, Konrad P E, Mager M, Mermel C H and Rapoport B I 2024 The Layer 7 Cortical Interface: A Scalable and Minimally Invasive Brain–Computer Interface Platform *bioRxiv* 2022.01.02.474656

[21] Konrad P, Gelman K R, Lawrence J, Bhatia S, Jacqueline D, Sharma R, Ho E, Byun Y W, Mermel C H and Rapoport B I 2025 First-in-human experience performing high-resolution cortical mapping using a novel microelectrode array containing 1024 electrodes *J. Neural Eng.* **22** 026009

[22] Cummins D D, Barth K, Ho E, Fink Skular A, Dister J, Rapoport B, Saez I and Bederson J B 2026 High-resolution cortical mapping within and across the central sulcus using 1024-electrode micro-electrocorticography arrays: illustrative case *J Neurosurg Case Lessons* **11** CASE25534

[23] Fischl B 2012 FreeSurfer *Neuroimage* **62** 774–81

[24] MacDonald D B, Dong C, Quatrale R, Sala F, Skinner S, Soto F and Szelényi A 2019 Recommendations of the International Society of Intraoperative Neurophysiology for intraoperative somatosensory evoked potentials *Clinical Neurophysiology* **130** 161–79

[25] Grundy B L 1982 Monitoring of sensory evoked potentials during neurosurgical operations: methods and applications *Neurosurgery* **11** 556–75

[26] Toleikis J R 2005 Intraoperative Monitoring Using Somatosensory Evoked Potentials: A Position Statement by the American Society of Neurophysiological Monitoring *J Clin Monit Comput* **19** 241–58

[27] Schreiner L, Jordan M, Sieghartsleitner S, Kapeller C, Pretl H, Kamada K, Asman P, Ince N F, Miller K J and Guger C 2024 Mapping of the central sulcus using non-invasive ultra-high-density brain recordings *Sci Rep* **14** 6527

[28] Gindrat A-D, Quairiaux C, Britz J, Brunet D, Lanz F, Michel C M and Rouiller E M 2015 Whole-scalp EEG mapping of somatosensory evoked potentials in macaque monkeys *Brain Struct Funct* **220** 2121–42

[29] Valencia M, Alegre M, Iriarte J and Artieda J 2006 High frequency oscillations in the somatosensory evoked potentials (SSEP's) are mainly due to phase-resetting phenomena *Journal of Neuroscience Methods* **154** 142–8

[30] Alkawadri R, Zaveri H P, Sheth K N and Spencer D D 2022 Passive localization of the central sulcus during sleep based on intracranial EEG *Cerebral Cortex* **32** 3726–35

Accepted Manuscript

[31] Ou Z, Guo Y, Gharibani P, Slepyan A, Routkevitch D, Bezerianos A, Geocadin R G and Thakor N V 2022 Time-Frequency Analysis of Somatosensory Evoked High-Frequency (600 Hz) Oscillations as an Early Indicator of Arousal Recovery after Hypoxic-Ischemic Brain Injury *Brain Sciences* **13** 2

[32] Navid M S, Niazi I K, Lelic D, Drewes A M and Haavik H 2019 The Effects of Filter's Class, Cutoff Frequencies, and Independent Component Analysis on the Amplitude of Somatosensory Evoked Potentials Recorded from Healthy Volunteers *Sensors* **19** 2610

[33] Dice L R 1945 Measures of the Amount of Ecologic Association Between Species *Ecology* **26** 297–302

Accepted Manuscript

Figures

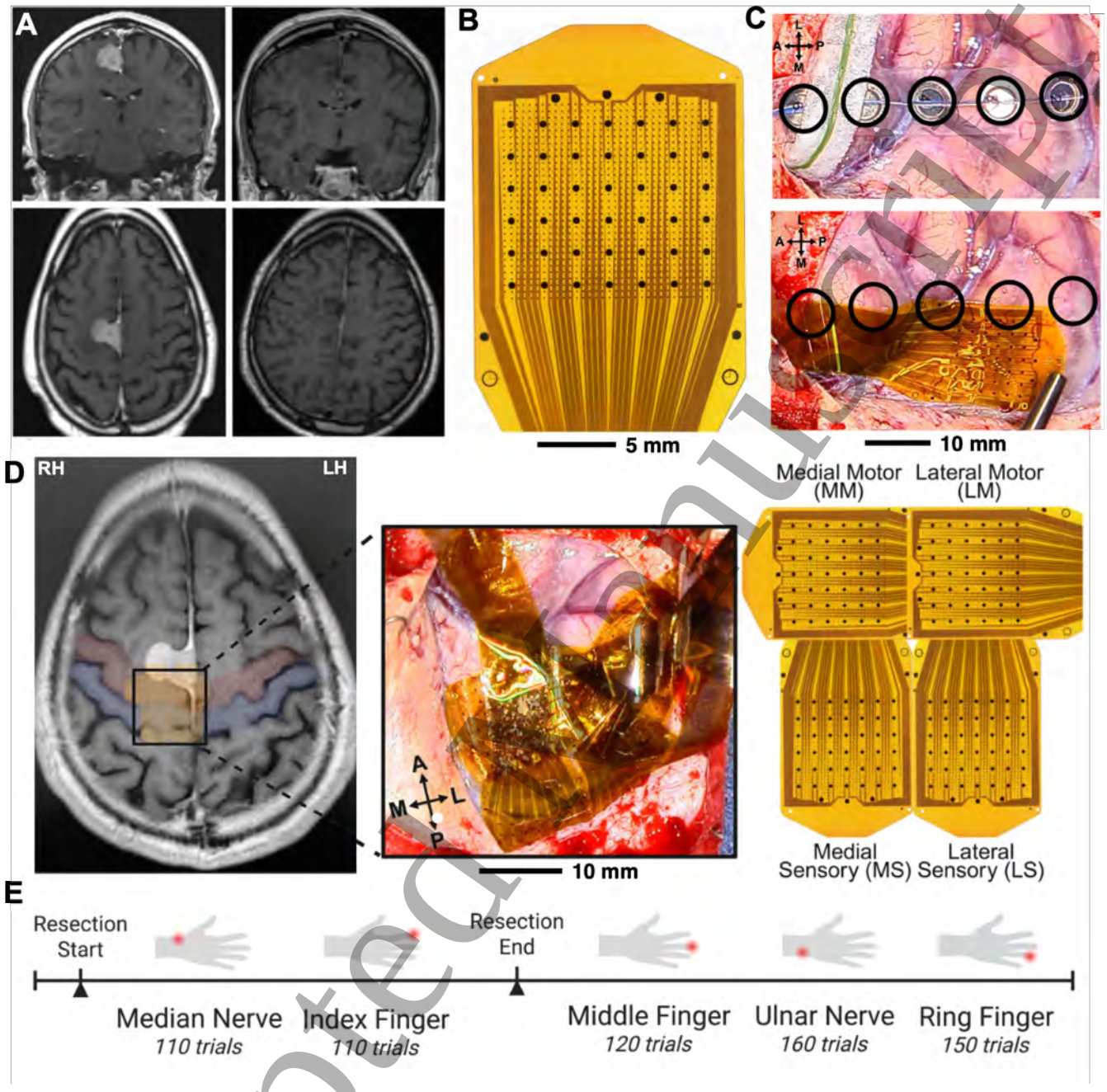


Figure 1. Intraoperative localization of the central sulcus and multi-array µECoG deployment during tumor resection. (**a**) Preoperative MRI demonstrating a 2-cm contrast-enhancing right parafalcine frontal mass with surrounding vasogenic edema (left), and postoperative MRI confirming gross total resection (right). (**b**) Schematic of the Layer 7 µECoG array, consisting of 1024 electrodes per array arranged in a 400 µm pitch grid spanning ~1.5 cm². Arrays are fabricated on a flexible polyimide substrate and include both recording (50 µm) and reference (up to 500 µm) electrodes. (**c**) Intraoperative comparison of electrode scale and spatial coverage. Top: cortical surface with an overlay of black circles marking the approximate position, ~4 mm diameter, and ~10 mm pitch of a standard 8-contact Ad-Tech subdural strip (Ad-Tech Medical Instrument Corporation, Oak Creek, WI). Bottom: same cortical surface with a 1024-channel Layer 7 µECoG array (visible yellow substrate) deployed over the same region, with the Ad-Tech footprint retained as black-circle overlay for scale reference. Scale bar = 10 mm for both. Anatomical compass (A = anterior, P = posterior, M = medial, L = lateral). (**d**) Final deployment configuration. Left: brain MRI rendering with the precentral gyrus (red), postcentral gyrus (blue), and the four-array footprint (yellow) overlaid. Middle: intraoperative photograph of the deployed Layer

Accepted manuscript

7 arrays *in situ*, with anatomical compass (A = anterior, P = posterior, M = medial, L = lateral). Scale bar = 10 mm. Right: schematic of the 2×2 array layout — medial motor (MM, top-left) and lateral motor (LM, top-right) horizontally on the exposed precentral gyrus; medial sensory (MS, bottom-left) and lateral sensory (LS, bottom-right) inserted vertically beneath the intact skull onto the dura overlying the postcentral gyrus, using a custom-built flexible stylet. Orientation differs between the sub-panels of (d): medial is to the right of the array box in the MRI rendering, but to the left in the intraoperative photograph and the schematic. (**e**) Stimulation protocol. Contralateral peripheral-nerve and digit stimuli were delivered sequentially: median nerve (n = 110 trials), index finger (n = 110), middle finger (n = 120), ulnar nerve (n = 160), and ring finger (n = 150). Median nerve and index finger stimulation occurred during tumor resection ("Resection Start" arrow); ulnar, middle, and ring stimulation occurred after gross total resection ("Resection End" arrow). Standard stimulation parameters: 1.41 Hz single-pulse frequency, 200 μs pulse width, 20–40 mA amplitude. A transistor–transistor logic (TTL) trigger was co-recorded with neural data for trial-averaging of stimulus-locked SSEPs.

Accepted Manuscript

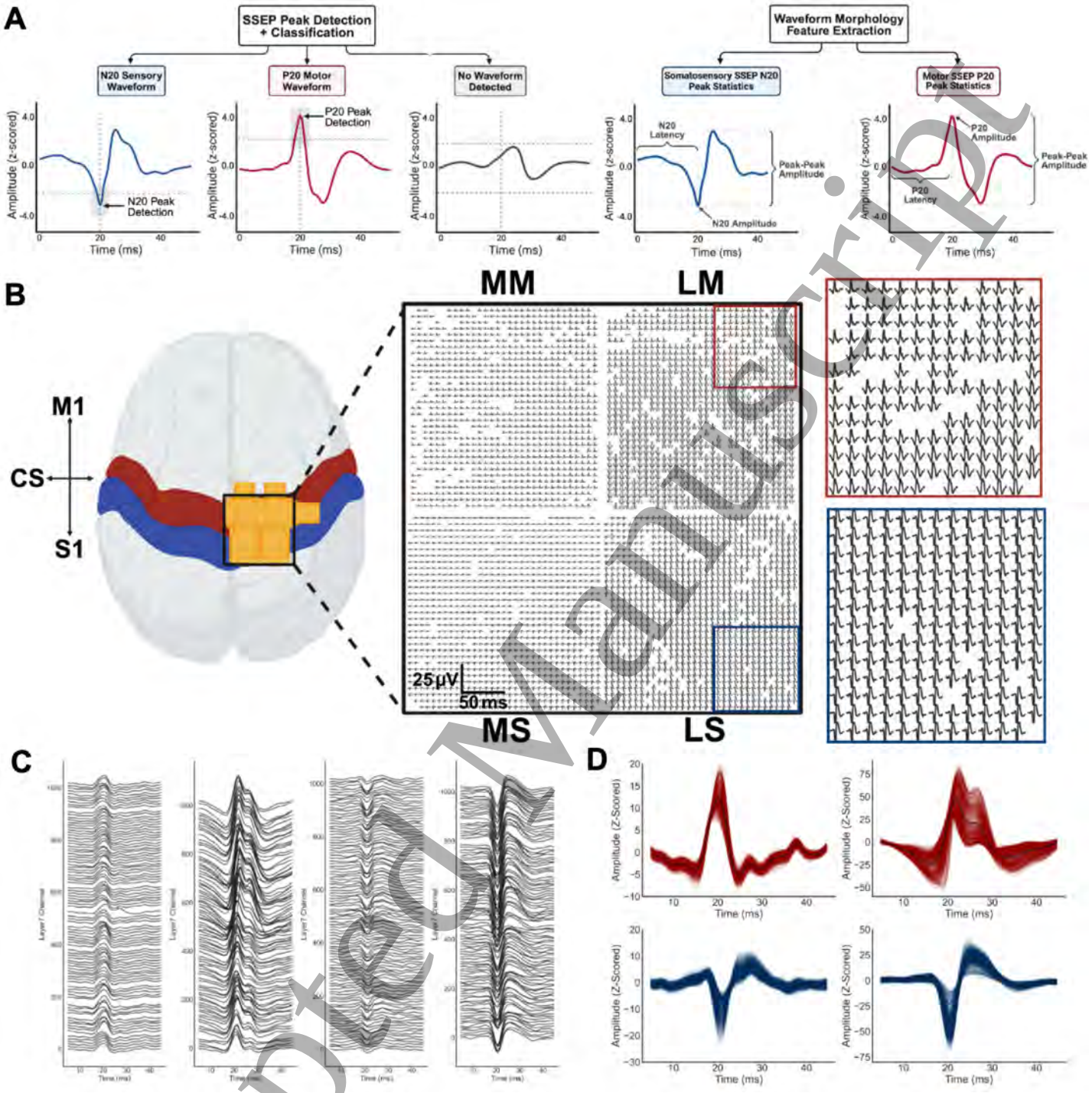


Figure 2. Automated SSEP detection and per-channel waveform classification across the four-array recording. (**a**) Workflow for detecting and classifying somatosensory evoked potentials (SSEPs) from high-density recordings. (**b**) Example median nerve-evoked SSEP waveforms from all four arrays: medial motor (MM), lateral motor (LM), medial sensory (MS), and lateral sensory (LS). Insets show zoomed waveforms for LM and LS arrays to highlight N20/P20 features. (**c**) Subset of SSEP waveforms plotted linearly for each array in the order: MM, LM, MS, LS. (**d**) Classification of SSEP features by polarity: blue traces represent N20-dominated waveforms; red traces represent P20-dominated waveforms. Top row: MM and LM; bottom row: MS and LS.

Accepted Manuscript

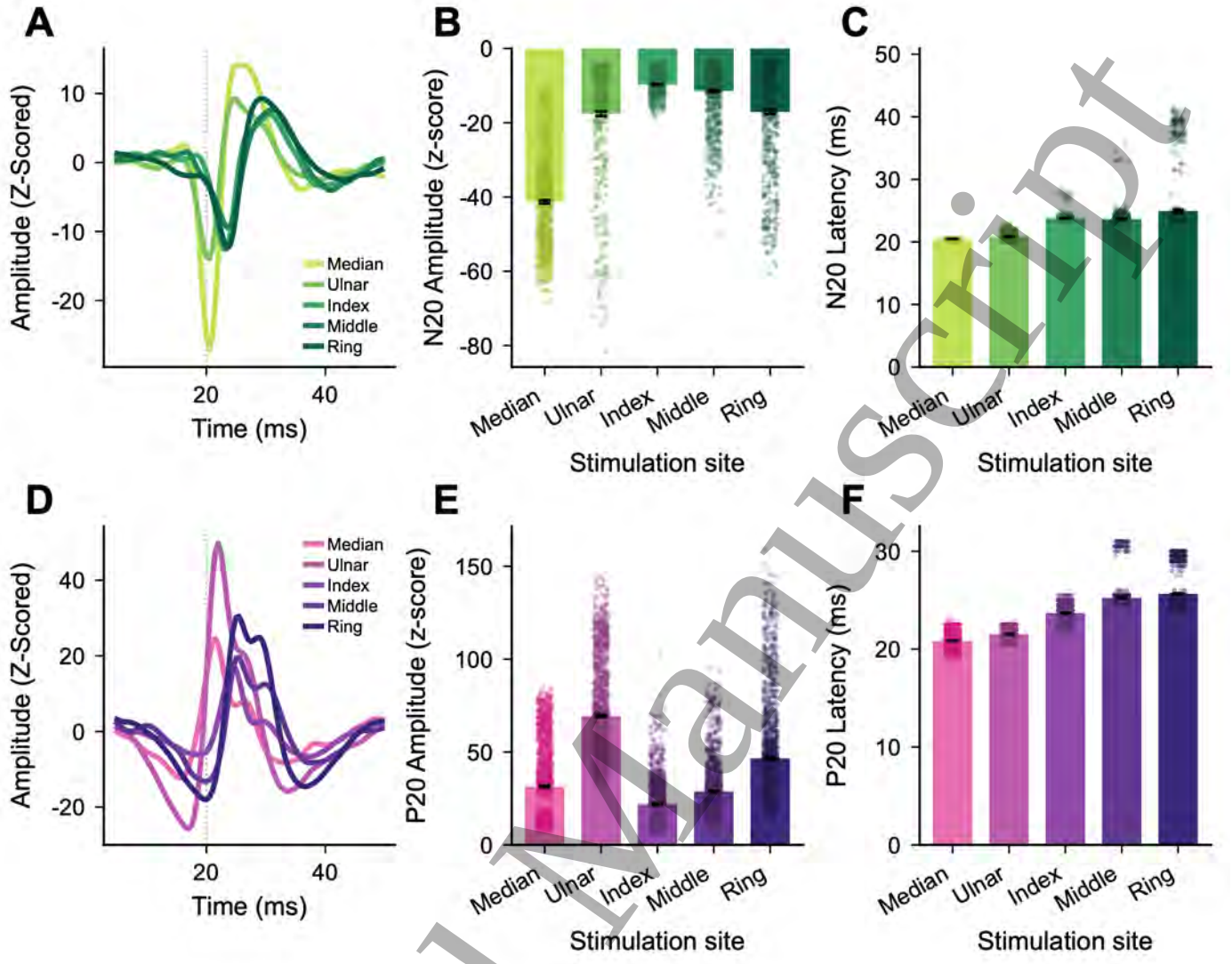


Figure 3. Per-stimulation SSEP morphology and peak features. Trial-averaged N20 and P20 SSEP morphology and extracted peak features, pooled across all classified channels of all four arrays, across the five stimulation conditions (median nerve, ulnar nerve, index finger, middle finger, ring finger). (**A**, **D**) Per-stimulation trial-averaged waveforms, pooled across all N20-dominant (A, green palette) or P20-dominant (D, purple palette) channels of all four arrays. Shaded ribbon = mean ± SEM across classified channels. (**B**, **E**) Mean ± SEM N20 (B) / P20 (E) peak amplitude in z-score units, with classified channels as observations. (**C**, **F**) Mean ± SEM N20 (C) / P20 (F) peak latency in ms, same channels and conventions. Individual classified channels are overlaid as jittered points in (B, C, E, F).

Accepted Manuscript

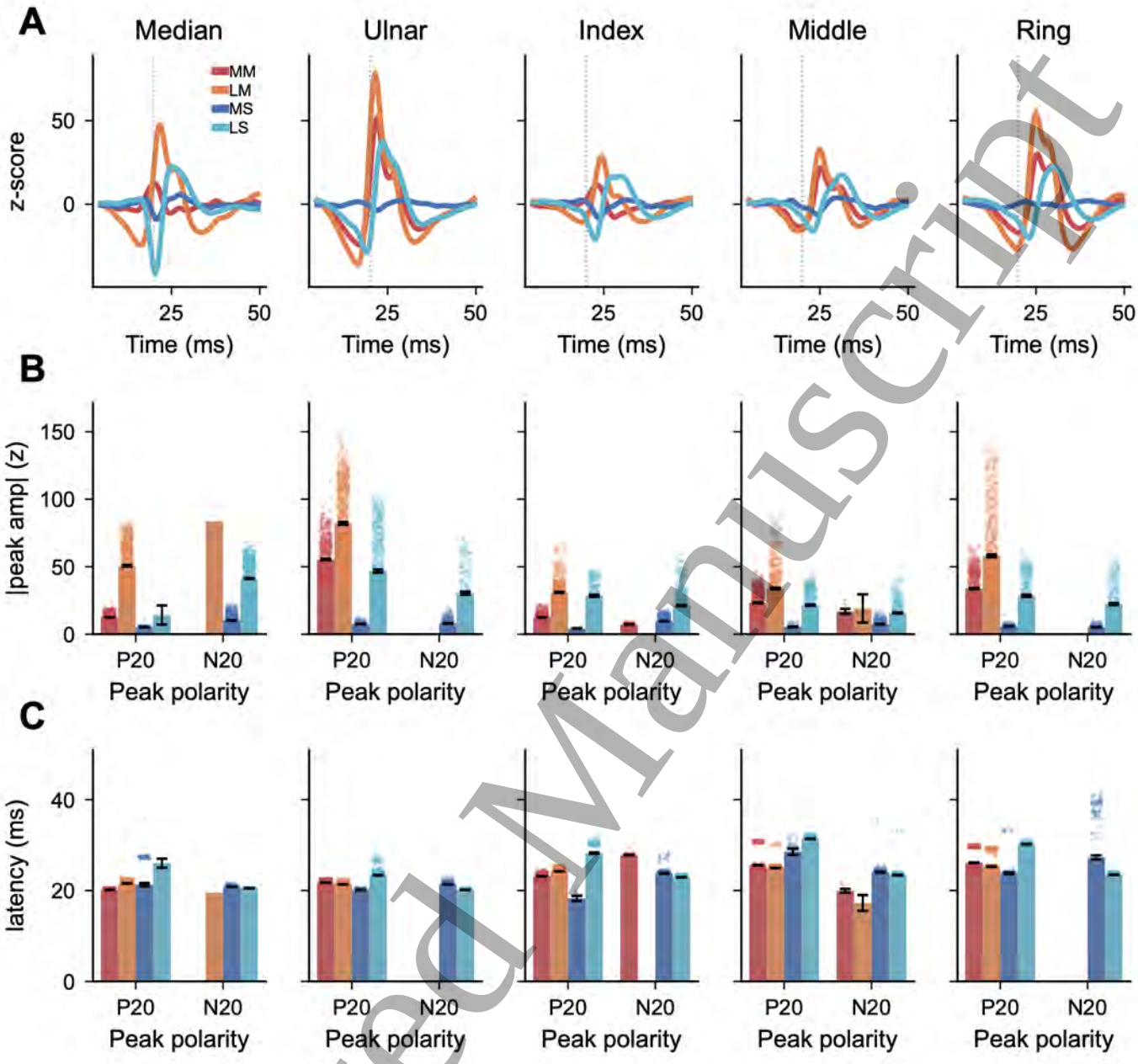


Figure 4. Per-array SSEP morphology and peak features stratified by stimulation condition. Per-array SSEP morphology, peak amplitude, and peak latency, across the five contralateral stimulation conditions. (**A**) Per-array somatosensory-evoked-potential (SSEP) waveforms for each stimulation condition (columns: Median, Ulnar, Index, Middle, Ring). Each trace is the mean across classified P20- or N20-dominant channels of the corresponding array; ribbon = ± SEM. Vertical dotted line at 20 ms marks the canonical P20/N20 timing reference. Array colors: MM (muted red), LM (amber), MS (slate blue), LS (light teal). (**B**) Per-array mean absolute peak amplitude (z-score) for the classified P20 and N20 channels at each stimulation condition (bars), with ± SD across channels (error bars). Empty bars indicate no classified channels of that polarity in that recording. (**C**) Per-array mean peak latency (ms) for the same P20 and N20 channels, same conventions. Individual classified channels are overlaid as jittered points in (B) and (C).

Accepted Manuscript

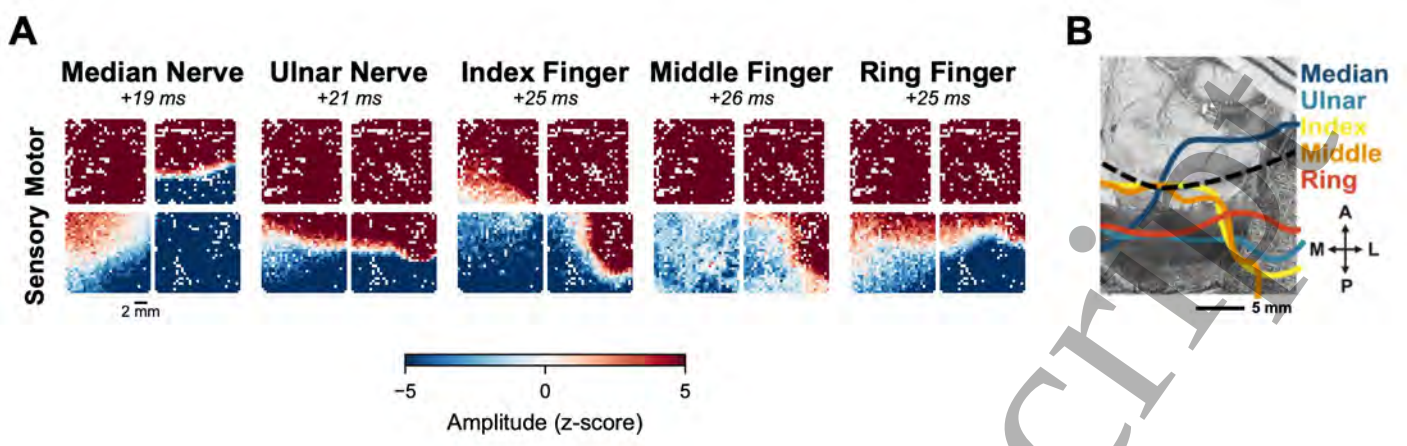


Figure 5. Per-electrode polarity at the central-sulcus phase-reversal latency. (**A**) Per-electrode SSEP amplitude (z-score) at the per-stimulation reported phase-reversal (PR) latency (median nerve, +19 ms; ulnar nerve, +21 ms; index finger, +25 ms; middle finger, +26 ms; ring finger, +25 ms), motor arrays (MM top-left, LM top-right) on top, sensory arrays (MS bottom-left, LS bottom-right) on the bottom. Each dot = one of 977 × 50 µm recording electrodes. RdBu_r color scale, ± 5 z-score saturation (colorbar, bottom). Scale bar = 2 mm. (**B**) Intraoperative photograph of the surgical field with the central sulcus (CS) marked by a dashed line, overlaid with the inferred per-stimulation PR contour (Median, Ulnar, Index, Middle, Ring). Anatomical compass: A = anterior, P = posterior, M = medial, L = lateral. Scale bar = 5 mm.

Accepted Manuscript

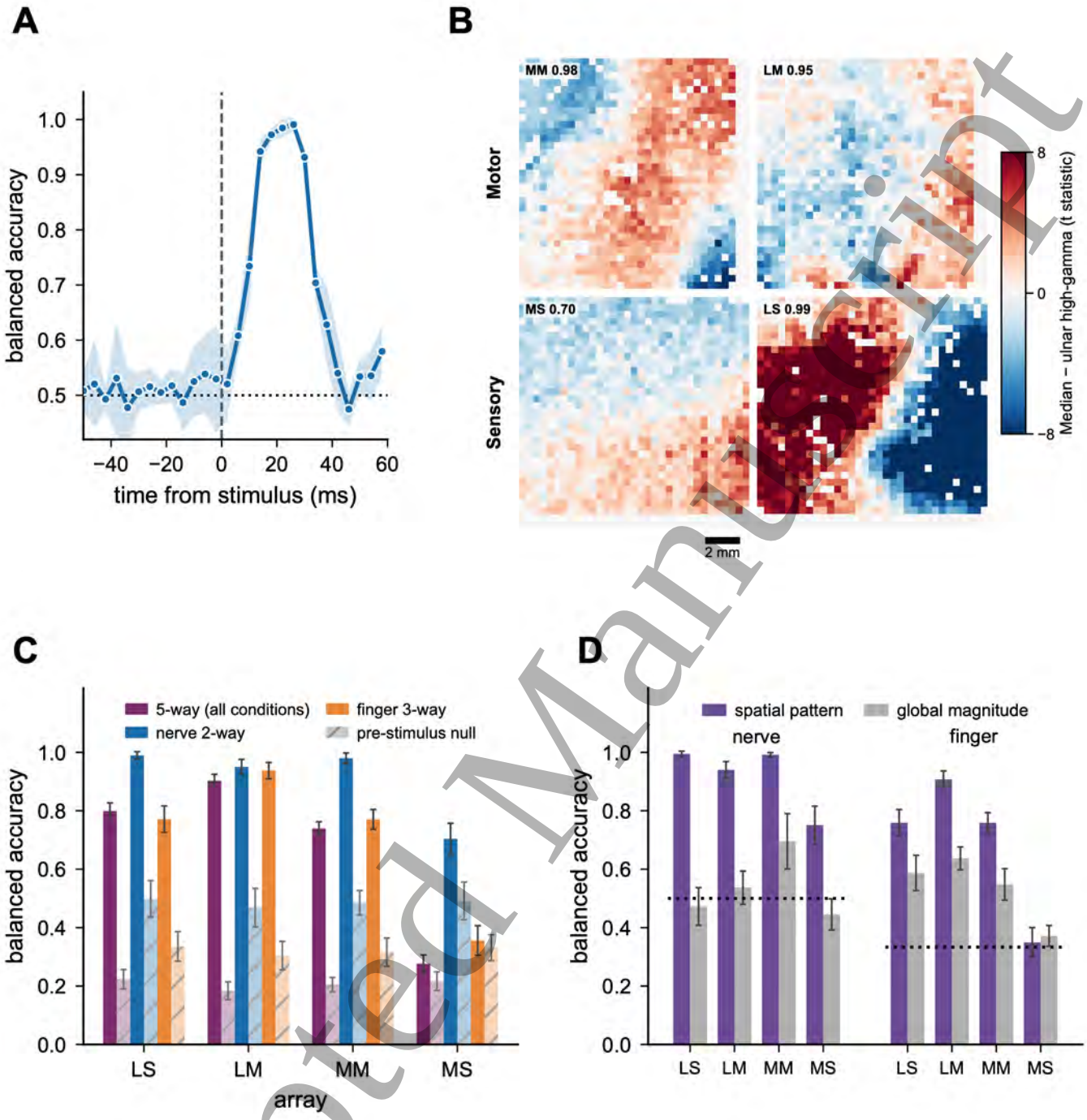


Figure 6. Single-trial spatial patterns distinguish stimulation conditions. For classification analyses, performance is reported as balanced accuracy, with error bars and shading showing ±1 SD across cross-validation folds. **(A)** Time-resolved median-versus-ulnar classification on the lateral sensory array. Performance was at chance before stimulation and increased during the evoked-response period, reaching 0.99 at +26 ms. Vertical dashed line marks stimulus onset; dotted horizontal line marks chance (0.50). The 15–32 ms response window used in the remaining panels is the interval over which accuracy rose above chance. **(B)** Per-channel median-minus-ulnar high-gamma contrast (Welch t statistic across trials) for each array, displayed at the physical electrode positions and arranged in the anatomical array layout used in Fig. 5A. Each tile is labeled with the array and its median-versus-ulnar balanced classification accuracy. Color scale is saturated at ±8; scale bar = 2 mm. **(C)** Balanced accuracy by array for five-condition classification (chance, 0.20), median-versus-ulnar classification (chance, 0.50), and three-digit classification (chance, 0.33). Hatched bars show performance

Accepted Manuscript

using features from the −24 to −4 ms pre-stimulus control window. **(D)** Classification based on the spatial response pattern versus global response magnitude for nerve and digit conditions. Spatial-pattern features were normalized within each trial to remove spatial mean and scale; global-magnitude classification used the whole-array mean response as a single feature. Dotted lines indicate chance (nerve, 0.50; digits, 0.33).

Accepted Manuscript

Stimulation Target	Peak-Peak Amplitude (z-score) (mean ± SD)	Peak-Peak Latency (ms) (mean ± SD)	N_{20} Peak Amplitude (z-score) (mean ± SD)	P_{20} Peak Amplitude (z-score) (mean ± SD)	N_{20} Peak Latency (ms) (mean ± SD)	P_{20} Peak Latency (ms) (mean ± SD)
Median Nerve	41.62 ± 13.12	13.13 ± 3.41	−41.29 ± 13.35	31.60 ± 9.24	20.49 ± 0.08	20.84 ± 0.45
Ulnar Nerve	62.73 ± 25.01	17.39 ± 6.38	−15.32 ± 10.46	68.69 ± 21.36	20.75 ± 0.38	21.54 ± 0.53
Index Finger	29.21 ± 11.19	13.44 ± 6.75	−9.71 ± 3.07	21.67 ± 6.74	23.77 ± 0.71	23.67 ± 0.56
Middle Finger	31.10 ± 13.65	17.52 ± 7.58	−9.62 ± 5.88	28.53 ± 11.68	23.75 ± 1.67	25.25 ± 1.25
Ring Finger	47.11 ± 22.20	16.13 ± 7.66	−11.17 ± 7.77	45.87 ± 20.36	24.00 ± 4.86	25.68 ± 1.78

Table 1. Per-stimulation peak features of automatically classified SSEP channels. Per-stimulation mean ± SD of peak-to-peak amplitude (z-score), peak-to-peak latency (ms), N20 peak amplitude (z-score), P20 peak amplitude (z-score), N20 peak latency (ms), and P20 peak latency (ms). Statistics are computed across all classified channels of all four Layer 7 arrays that passed the 2 MΩ impedance criterion. Amplitudes are unitless z-scores computed against the per-channel pre-stimulus baseline window (−80 to −30 ms); latencies are post-stimulus.

Accepted Manuscript